CHAPTER 4

SYNTHESIS AND CHARACTERISATION OF CARBON AEROGEL

4.1 Synthesis of Carbon Aerogel derived from Carboxymethyl Cellulose

CA was derived from commercial grade CMC by preparing 4% of CMC solution and then mixing it with several metal ion solutions to form CMC hydrogel. Metal ions played an important role in CMC aerogel structure as a bridge for the crosslinking network or crosslinking agent, but different metal ions contributed to the formation of different structures of CMC aerogels. In this study, four selected metal ions, magnesium ion (Mg^{2+}), manganese ion (Mn^{2+}), nickel ion (Ni^{2+}), and zinc ion (Zn^{2+}) coming from two different groups of metals, alkaline earth metals and transition metals, were investigated. Mg^{2+} belonged to alkaline earth metals, while Mn^{2+}, Ni^{2+}, and Zn^{2+} belonged to transition metals.

Moving across the element period of the periodic table, Mg^{2+} was selected first due to its larger size compared to the other metals that caused it to be more reactive than Mn^{2+}, Ni^{2+} and Zn^{2+}. Besides, Mn^{2+}, Ni^{2+}, and Zn^{2+} were chosen because the increased number of their protons exerted a stronger positive charge. With this consideration, these metals were expected to take full advantage of CMC as a crosslinking agent and form a CMC aerogel with better properties. Generally, all CMC aerogels were white in colour but formed different structures (Figure 4.1). The nature of the metal ions used affects the formation of CMC aerogels, thus showing a significant difference between these two groups. A hard and fragile structure was observed for Mn^{2+}, Ni^{2+} and Zn^{2+}. In contrast, a well-developed spongy structure of

CMC-Mg was observed due to the efficient crosslinking reaction or gelation process occurred between Mg^{2+} and CMC.

a) Mg^{2+} b) Mn^{2+}

c) Ni^{2+} d) Zn^{2+}

Figure 4.1: Condition of CMC Aerogels Treated with Different Types of Metal Ions a) Mg^{2+} b) Mn^{2+} c) Ni^{2+} and d) Zn^{2+}

Generally, the special feature of CMC is the occurrence of crosslinking reaction when added with any cation and lead to the formation of hydrogel solution. As shown in Scheme 4.1, NaCMC is the starting precursor and Mg^{2+} acts as a crosslinking agent to induce the formation of crosslinking network between CMC and Mg^{2+}. The large amount of carboxylate groups on CMC molecular chains have made Mg^{2+} to react with the carboxylate group to form crosslinked network structure

(Yu et al., 2017). The reaction forms hydrogel solution and the solutions are freeze-dried to obtain CMC aerogel.

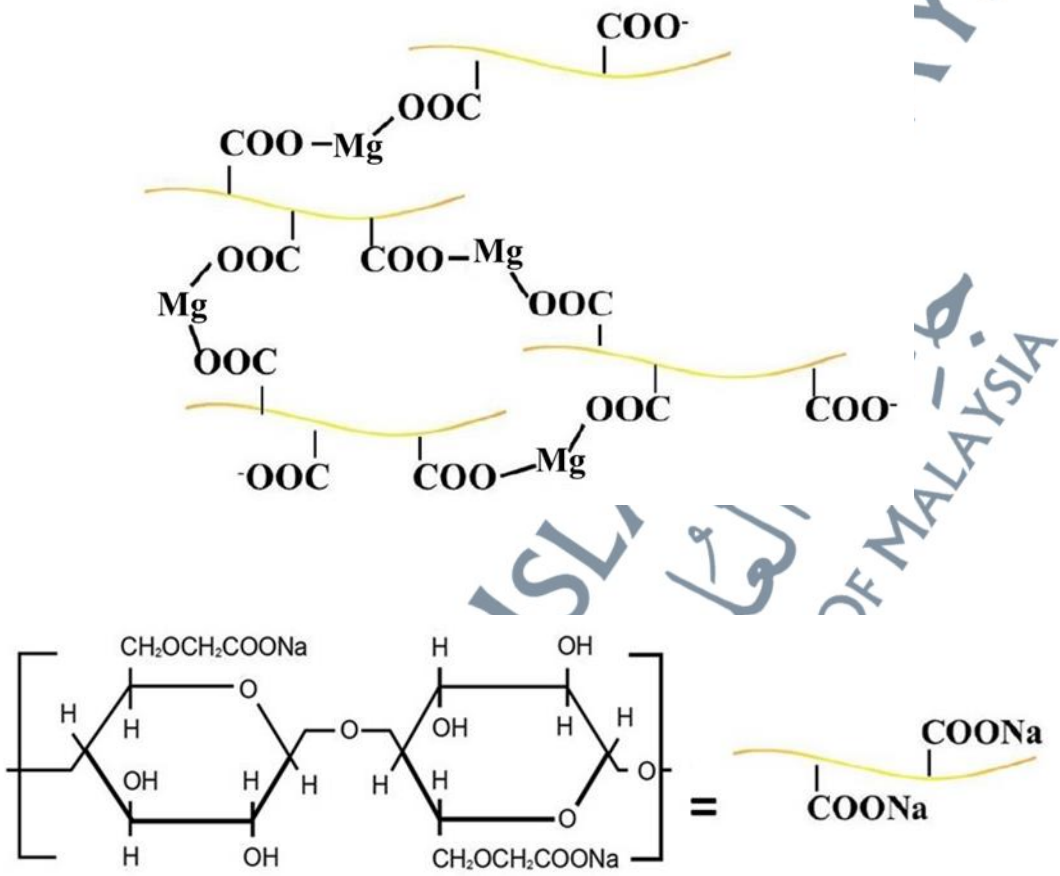

Scheme 4.1: Crosslinking Reaction of CMC-Mg Aerogels

4.1.1 Effects of Metal Ions Concentration

In the present study, the formation of CMC hydrogel at different concentrations (0.002, 0.004, 0.006, 0.008, and 0.01 mol) for each metal ions were investigated. The crosslinking reaction started to occur and formed hydrogel solution or gel-like solution after the addition of metal ions solution with CMC solution during gelation process. During carbonisation, the samples experienced loss in weight and

all the changes were tabulated in Table 4.1. The samples weights were calculated and determined based on the mole ratio of the metal ions in the samples. The ratio was derived from the molecular weight (g/mol) of the samples, with the mole as a constant variable throughout the research. The mole value represented the concentration of the metal ions, which were set at 0.002, 0.004, 0.006, 0.008 and 0.01 mol. Each sample had been repeated several times with consistent times and consistent percentage of weight loss was recorded. The relative standard deviation (RSD) was calculated to determine the data precision. The RSD of the samples data was deemed acceptable (≤ 5). A smaller RSD value indicated higher precision in the data. The utilisation of 90% confidence intervals was appropriate due to inconsistent RSD values in some of the data. However, the RSD values remained small, indicating that the sample data exhibited minimal dispersion.

Table 4.1: Percentage Weight Loss of Samples

Concentration (mol)	**Average Percentage Weight Loss (%)**			
	CA-Mg	**CA-Mn**	**CA-Ni**	**CA-Zn**
0.002	53.55 ± 4.80	60.59 ± 2.35	61.93 ± 3.07	71.63 ± 3.63
0.004	56.55 ± 4.40	65.74 ± 4.29	59.18 ± 3.67	62.41 ± 2.82
0.006	58.56 ± 4.11	68.85 ± 3.62	0	72.36 ± 3.78
0.008	58.60 ± 1.97	0	0	0
0.01	64.07 ± 4.53	0	0	0

*Percentage weight loss for pure CA: 64.54%

As shown in Table 4.1, the weight loss of pure CA is calculated to be 64.54% due to the pyrolysis of carbon. At 0.002 mol, the percentage weight loss of CA-Mg (53.55%), CA-Mn (60.59%), and CA-Ni (61.93%) were below the percentage weight loss of pure CA, and only CA-Zn (71.63%) exceeded the percentage value. This indicates the presence of Mg, Mn, and Ni was significant in reducing the weight loss of CA during the carbonisation process. At 0.004 mol, only CA-Mn (65.74%) exceeds the weight loss of pure CA, while CA-Mg (56.55%), CA-Ni (59.18%), and CA-Zn (62.41%) do not exceed the weight loss of pure CA. At 0.006 mol, only CA-Mg (58.56%) was recorded below the weight loss of pure CA as compared to CA-Mn (68.85%) and CA-Zn (72.36%), while CA-Zn was totally lost. The percentage weight loss was only calculated for CA-Mg at 0.008 and 0.01 mol with a value of 58.60% and 64.07%, respectively, while CA-Mn, CA-Ni, and CA-Zn were totally lost after the carbonisation process. Each CAs was carbonised with temperatures up to 800 °C that caused any volatile substances to be removed first as the temperature kept increasing. The rapid loss of weight for CA-Mn, CA-Ni and CA-Zn at certain concentrations may be caused by the compact agglomeration of the metal oxide nanoparticles (MnO, NiO, ZnO). This can be observed based on the increase of the average particle size and decrease of the specific surface area which occurred when the concentration was increased (Baharudin et al., 2018).

The percentage weight loss of the samples increased as the concentration of metal ions increased, owing to the decomposition of an anion that acted as an oxidizing agent for the CA (Ji et al., 2020). Besides, the presence of Mg in the crosslinking structure of CA is stable because the percentage weight loss at all concentrations was below the weight loss of pure CA. Furthermore, the increasing rate of weight loss was promising, as Mg^{2+} played a big role in reducing weight loss

even though the concentration kept increasing.

At this point, the data obtained shows that alkaline earth metals were suitable as enhancers for the synthesis of CA compared to the other transition metals due to their stability and promising results. The nature of the metal ions used in the synthesis of CA is important because it could affect the structure and morphology of the CA obtained. Therefore, for further analysis, CA-Mg samples were selected for the characterisation of CA because they could be the best candidate for hydrogen storage materials.

4.2 Characterisation of Carbon Aerogel

The samples of CA-Mg were further analysed to characterise their structure and morphology based on FTIR, XRD, BET and FESEM analysis. The data were recorded and discussed as below:

4.2.1 Completion of Carbonisation

In this research, FTIR analysis was carried out for CMC-Mg, pure $MgCl_2$, CA, and CA-Mg samples (Figure 4.2) to compare the spectra before and after the carbonisation process, indicating the completion of CA carbonisation based on the disappearance of OH group. The CMC-Mg was produced from the crosslinking reaction between NaCMC and $MgCl_2$. The presence of OH stretch was exhibited at 3356 cm^{-1} and 3371 cm^{-1} for pure $MgCl_2$ and CMC-Mg, respectively (Figure 4.2). The FTIR spectra of CMC-Mg and $MgCl_2$ observed were similar, with the presence of the -OH and C=C functional groups in both samples. However, the transmittance decreased after the sol-gel process, where CMC was crosslinked with Mg^{2+}, as shown in Scheme 4.1. Therefore, it proved the occurrence of the crosslinking reaction that

led to the formation of the hydrogel solution, CMC-Mg (Pandey et al., 2020).

After carbonisation, the CMC-Mg was converted into CA-Mg, and the spectra showed the loss of the -OH and C=C functional groups. Compared to pure CA, the functional groups of -OH and -CO were still present even after the carbonisation process. This is because the crosslinking of CMC with Mg^{2+} has not occurred yet and carbonisation of pure CA is incomplete. With the addition of Mg^{2+}, the carbonisation became complete because fewer peaks were observed in the FTIR spectra compared to pure CA, as shown in Table 4.2.

Table 4.2: IR Data of Samples

Samples	Wavenumber (cm^{-1})	Group
$MgCl_2$	3331	O-H stretching (alcohol)
	1607	C=C stretching (cyclic alkene)
CMC-Mg	1051	C-O stretching (primary alcohol)
	1586	C=C stretching (cyclic alkene)
	1412	O-H bending (carboxylic acid)
CA	3398	O-H stretching (alcohol)
	1100	C-O stretching (aliphatic ether)
	620	none
CA-Mg	-	-

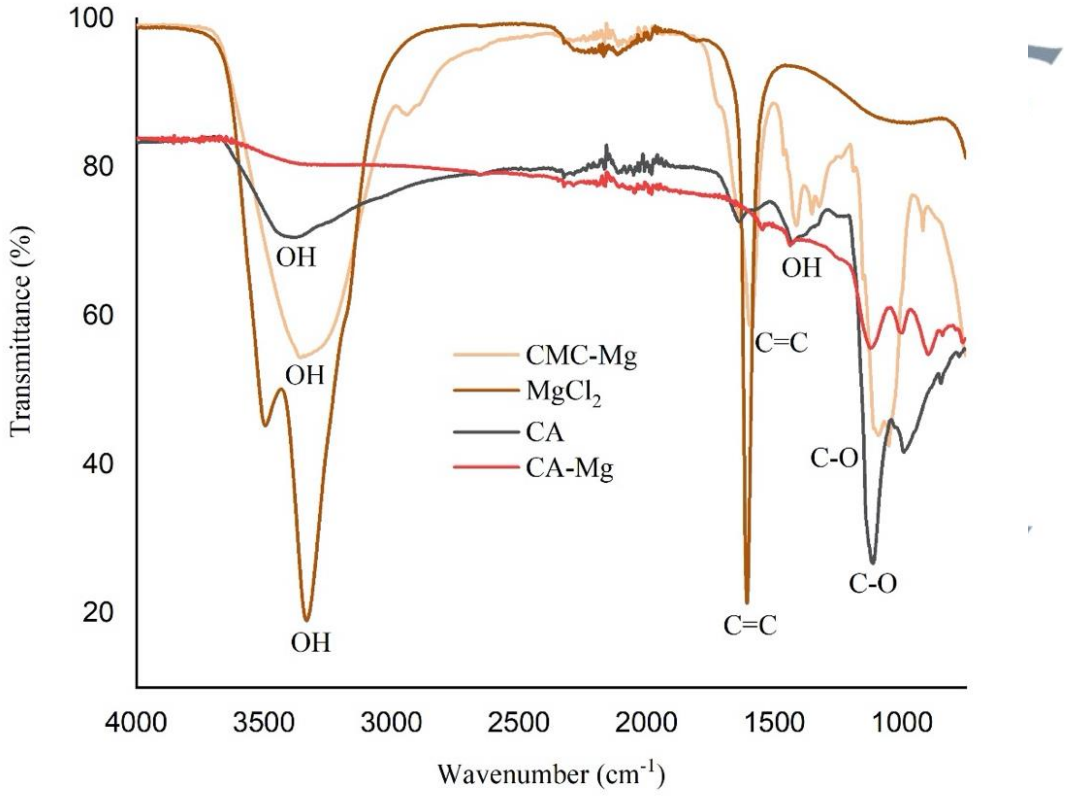

Figure 4.2: FTIR Spectra of CMC-Mg, $MgCl_2$, CA and CA-Mg

4.2.1.1 FTIR Spectra of CA-Mg at Different Concentrations of Mg^{2+}

Figure 4.3 shows the FTIR spectra of pure CA and CA-Mg at different concentrations of Mg^{2+} (0.002, 0.004, 0.006, 0.008, and 0.01 mol). The IR spectrum of pure CA shows the presence of the -OH stretch at 3332 cm^{-1} and the -CO stretch at 1100 cm^{-1} while no peak was present for CA-Mg, indicating that either the $MgCl_2$ became anhydrous or decomposed to another compound. This can be clearly seen on the FTIR spectra of CA-Mg at 0.002 mol at the same transmittance reading as with pure CA. As the concentration of Mg^{2+} increased to 0.01 mol, the transmittance percentage of CA-Mg decreased and did not show any significant peaks because most of the functional groups that exist in CMC-Mg were decomposed during the

carbonisation process. Thus, the presence of Mg^{2+} played a big role in promoting the complete carbonisation of CA.

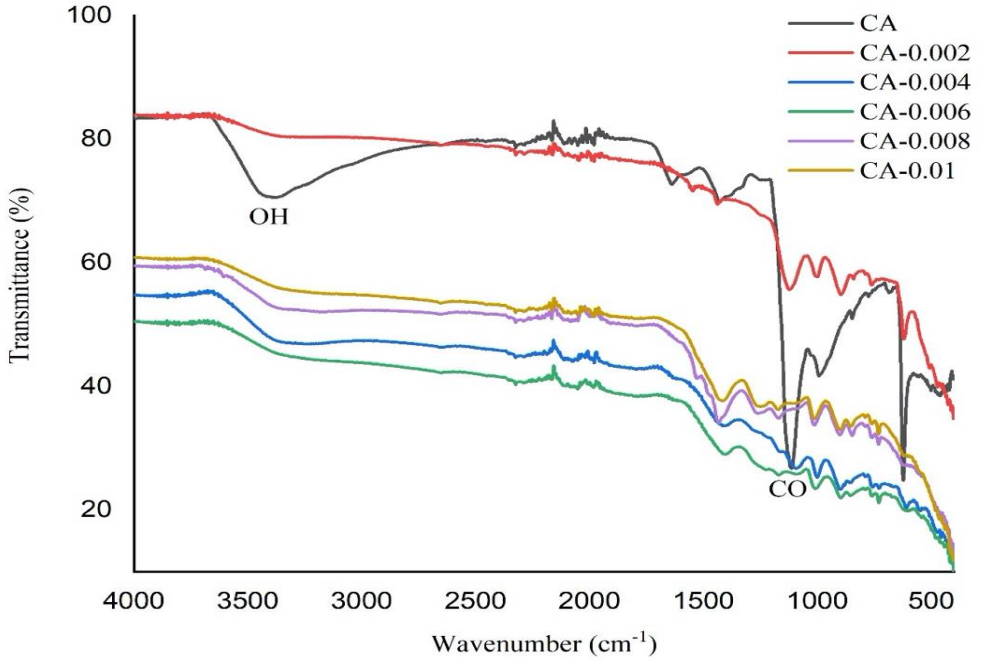

Figure 4.3: FTIR Spectra of Pure CA and CA-Mg with Different Concentrations of Mg^{2+} after Carbonisation

4.2.2 Disappearing of OH

The crystalline structure of the CA-Mg samples was analysed by using X-ray powder diffraction (XRD) spectroscopy. Figure 4.4 represents the XRD patterns of CA-Mg samples in the 2-theta range of 20° - 90°. The samples were tested with five different concentrations of Mg^{2+} (0.002 mol, 0.004 mol, 0.006 mol, 0.008 mol and 0.01 mol) and similar patterns were observed representing the characteristics of a highly crystalline compound. Based on the pattern, the diffraction peaks of MgO (Periclase) emerged at 2 thetas of 39°, 45.5°, 66.2°, 79.7° and 84° showing the crystalline phase of MgO, which can be indexed as the (111), (200), (220), (311) and (222) lattice planes. The determination of the diffractogram peak was based on the XRD profile pattern of periclase. Periclase (MgO) is the only existing crystalline form of MgO (Dercz et al., 2009).

MgO was generated during carbonisation process of CA-Mg samples. During the crosslinking reaction, $MgCl_2$ reacted with the carboxylate group of CMC structure and formed a crosslinked network structure of CMC-Mg. Then, it decomposed into MgO during carbonisation. Hence, this is the reason for the disappearing OH peak in the FTIR spectra depicted in Figure 4.2. Thus, the sample was proven to have characteristic features of CA and MgO. The concentration of Mg^{2+} was influential in the formation of MgO and led to a slight increase in peak intensity. Besides, the peak intensity may not be visible in the XRD pattern at low concentrations such as at (111) and (311).

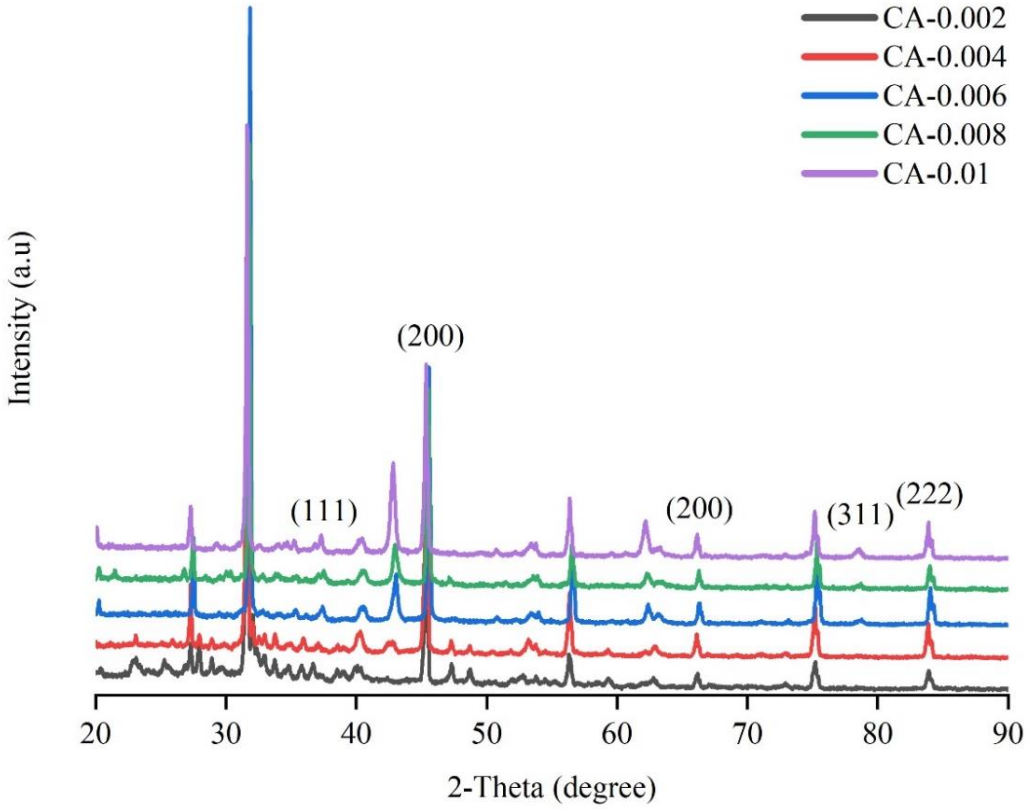

Figure 4.4: XRD Patterns of CA-Mg Samples with Different Concentration (0.002, 0.004, 0.006, 0.008, 0.01) mol

From the XRD data, the crystallite size of CA-Mg samples was calculated by using the Scherrer equation (also known as the Debey-Scherrer equation) as shown below:

$$L = \frac{K\lambda}{(FWHM)\ Cos\theta} \quad (4.1)$$

FWHM = Full Width Half Maxima

K = Shape factor, constant

λ = wavelength of x-ray used

L = particle size

$\cos\theta$ = peak position ($2\theta/2$) in radian

The XRD peak of 200 lattice planes was chosen to calculate the crystallite size for each of the concentration by using the equation above, but there was a limitation on the crystallite size. This equation applicable only to small crystallites size (≤ 100 nm). The data summary for CA-Mg samples was tabulated as shown in Table 4.3.

Table 4.3: Summary of XRD Peak Position and Full Width Half Maxima (FWHM) of CA-Mg at 200 Lattice Planes

Concentration (mol)	FWHM (°)	Crystallite Size (nm)
0.002	0.26529	33.94
0.004	0.19833	45.40
0.006	0.17506	51.44
0.008	0.17428	51.67
0.01	0.19442	46.31

From Table 4.3, the data showed that the crystallite size of the CA-Mg samples were below ≤ 100 nm, which is fine data for Scherrer equation. The

crystallite size of CA-Mg samples was based on the size of MgO as the XRD detected the presence of highly crystalline compound (MgO) in the CA-Mg samples (Figure 4.5). The size of MgO was calculated based on MgO (periclase) indexing. At 0.002 mol, the crystallite size was the lowest (33.94 nm) and experienced a sudden increase in size (45.40 nm). The biggest crystallite size was at 0.008 mol (51.67 nm) and decreased slightly at 0.01 mol (46.31 nm). The crystallite size of the samples was getting bigger as the concentration of Mg increased, showing the significant role of metal ions in synthesising the best CA. Besides, XRD peak at 200 lattice planes, or 45.5° of 2θ was chosen because in the analysis of single peaks, peaks between 30° and 50° of 2θ was often offered a better result.

4.2.3 Pore Structural and Specific Capacity of Carbon Aerogel

The Nitrogen (N_2) adsorption/desorption experiments were performed on pure CA and CA-Mg samples using BET methods to investigate the specific surface area and pore size distribution of the pure CA and CA-Mg samples (Figure 4.6). According to IUPAC classification, each of the sample exhibited typical types of IV adsorption/desorption isotherms. This analysis was carried out in the relative pressure region of $0.4 < P/P_o > 1.0$, where each sample displayed a clear hysteresis loop in that region, showing the existence of mesopores (pore sizes 2-50 nm) as shown in Figure 4.5.

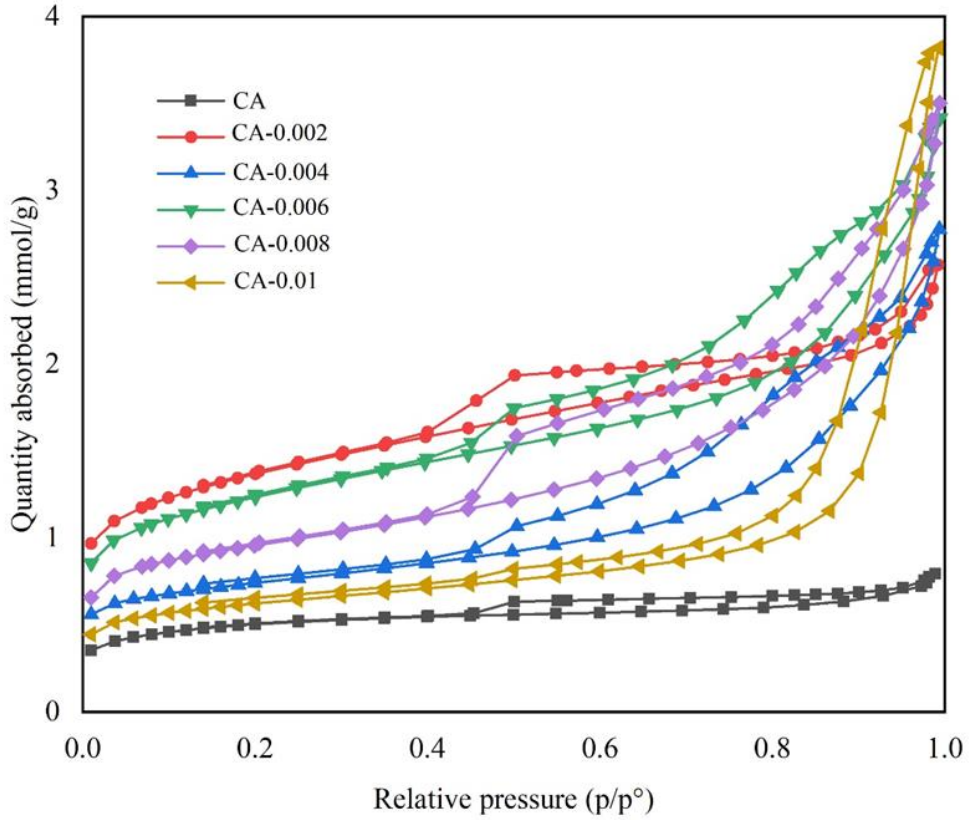

Figure 4.5: Nitrogen Adsorption/Desorption Isotherms of Pure CA and CA-Mg Samples with Different Concentrations (0.002, 0.004, 0.006, 0.008, 0.01 mol)

The pore structural parameters and specific capacities of the pure CA and CA-Mg samples were tabulated, and the contribution of micropores (pore sizes up to 2 nm) was calculated as shown in Table 4.4. The CA-0.002 sample showed a maximum specific surface area of 101.4407 m^2/g which will probably become a factor in the increased occurrence of the cross-linking reaction and lead to the formation of many pores during the carbonisation process. The pure CA sample exhibited the lowest pore volume of 0.0275 cm^3/g, whereas the CA-Mg samples for 0.002, 0.004, 0.006, 0.008, and 0.01 mol displayed larger pore volumes of 0.0893, 0.0965, 0.1186, 0.1216, and 0.1327 cm^3/g respectively. However, an anomaly was

observed at 0.004 mol, where the micropore volume experienced a sudden decrease. This phenomenon can be attributed to the compact agglomeration of MgO nanoparticles, potentially resulting in an increase in average particle size and a decrease in specific surface area (Baharudin et al., 2018). Based on Table 4.4, the micropore volume of CA contributed 29.9% of the pore volume, while for CA-0.01, the contribution of the micropore was 7.5% of the pore volume. The CA-0.01 sample possessed the highest value of pore volume, which is 0.1327 cm^3/g and the most probable pore size of 11.6339 nm. These features of CA-0.01 could offer a good adsorption site for hydrogen gas and act as a potential candidate for a hydrogen storage material (Mehrabi et al., 2019).

Table 4.4: The Pore Structural Parameters and Specific Capacity of the CA and CA-Mg Samples

Samples	S_{BET} (m^2/g)	S_{mic} (m^2/g)	V_{total} (cm^3/g)	V_{mic} (cm^3/g)	Contribution of Mic (%)	D (nm)
CA	36.3241	15.1654	0.0275	0.0082	29.9	3.0379
CA-0.002	101.4407	33.6572	0.0893	0.0179	20.1	3.5240
CA-0.004	54.3267	23.6874	0.0965	0.0124	12.9	7.1064
CA-0.006	91.8824	29.9439	0.1186	0.0158	13.4	5.1644
CA-0.008	70.6374	27.7358	0.1216	0.0145	11.9	6.8913
CA-0.01	45.6454	18.6878	0.1327	0.0098	7.5	11.6339

In addition, pore size was the main parameter in analysing the best adsorption site for hydrogen gas since it had a great influence on total pore volume, as shown in

Figure 4.6. Higher total volume of pore contributed to high possibility of hydrogen gas to adsorb at the CA samples. The increase in pore size caused an increase in total pore volume, which consists of micropores and mesopores. In obtaining the best adsorption site for hydrogen gas, the presence of mesopores was required and can be determined based on the hysteresis loop as shown in Figure 4.5. The micropore volume decreased as the total pore volume increased. Thus, it proved the presence of other pores, especially mesopores, which was a possible feature of hydrogen storage materials. Furthermore, the abnormality in the figure trend was observed at a pore size of 7.106 nm (CA-0.004), where there was sudden decreased of the sample's pore volume. Once again, this can be attributed to the impact of the compact agglomeration of MgO nanoparticles (Baharudin et al., 2018).

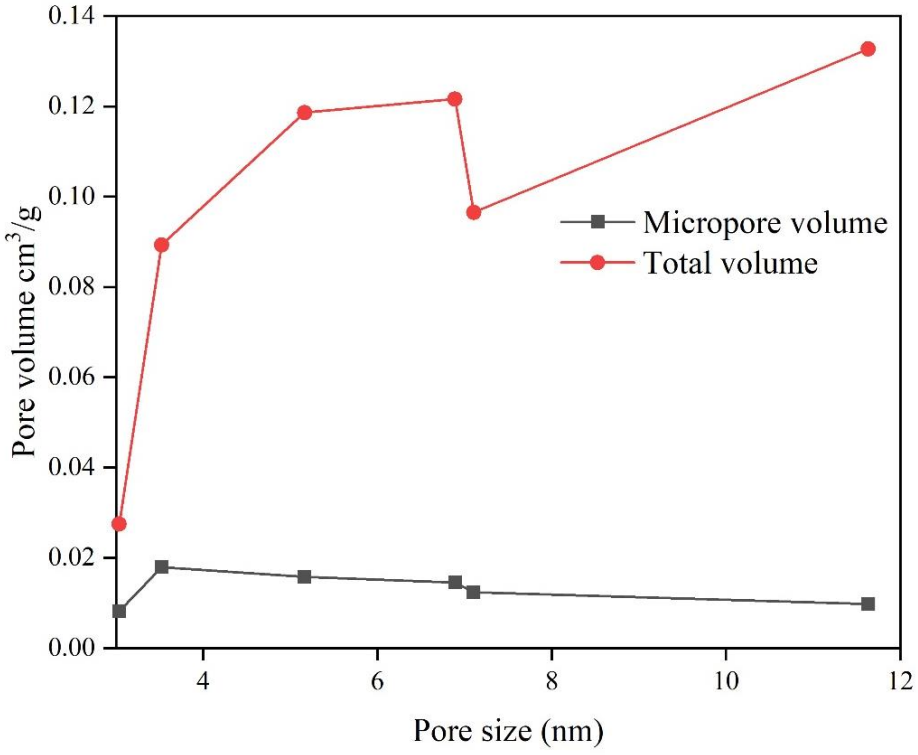

Figure 4.6: Influence of Pore Size (nm) towards Total Pore Volume (cm^3/g) of CA Samples

4.2.4 Glimpse of Carbon Aerogel Pore Shape

Other than specific pore volume, specific surface area, and pore size, BET analysis can provide information about microporous materials in terms of pore shapes. The presence of hysteresis loops in Figure 4.5 represents the presence of mesopores. Hysteresis happened in the multilayer range of physisorption isotherms, which is usually related to the condensation inside the capillaries of mesoporous structures (Calzaferri et al., 2023). The hysteresis loops can be divided into two types: extreme loops and intermediate loops. Types H1 and H4 were assigned to the extreme loop while types H2 and H3 were assigned to the intermediate loop (Thommes et al., 2015).

In type H1, the two branches were almost vertical and almost parallel over a wide range of gas uptake. Type H1 was often related to porous materials with the shape of a cylinder. In type H4, the branches stayed nearly horizontal and parallel over a wide p/p^o range and represented porous materials with narrow slit-shaped pores. For the intermediate loop, type H1 gave rise to type H2 where the pore size and pore shape distribution were not well-defined, as type H2 was often related to porous materials with ink- bottled shape pores. For the H3 loop, the materials started to possess slit-like shape pores. These classifications of hysteresis loops and their related pore shapes are shown in Figure 4.7.

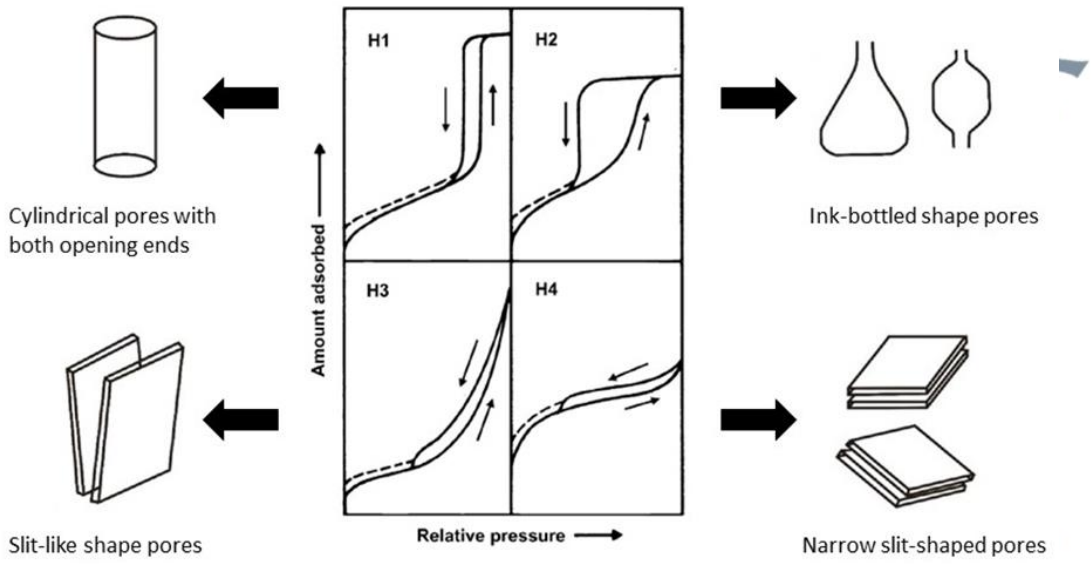

Figure 4.7: Classification Type of Hysteresis Loops and Their Related Pore Shapes

As shown in Figure 4.8, the N_2 adsorption/desorption isotherms of pure CA and CA-Mg samples can be classified based on their hysteresis loop type. Their related pore shape can be determined from the hysteresis loop type based on the classification in Figure 4.7. For pure CA, it showed characteristics of type H4 loops where the pore was narrow slit-shaped pores. Then, when the CA was enhanced with Mg^{2+} at 0.002, 0.004, 0.006, and 0.008 mol, the loops represented the H2 type, and the pore shape was not well-defined, usually like an ink-bottled shape pore. At 0.01 mol, the loop represented H3 loop where the pore become slit-like shape pore.

The pore shapes were changed when crosslinked with Mg^{2+}. The contribution of the mesopore in the samples was the highest at 0.01 mol, which explains why starting from this concentration, the pore shape of the CA-Mg sample was possibly a slit-like shape pore. This is presented in Table 4.4 where the contribution of micropores was 7.5% and has almost completely disappeared. The

summary of glimpse of pore shape of pure CA and CA-Mg samples is shown in Table 4.5 where the changes of the pore shape can be seen clearly as the concentration of Mg^{2+} increases. The pore changes were further analysed and observed using FESEM images as reported in 4.2.5.

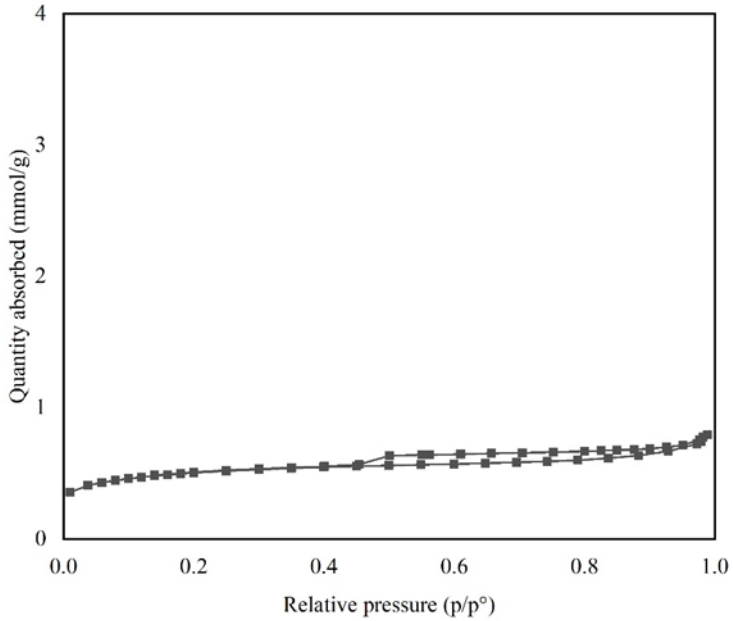

a) Pure CA: H4 loop

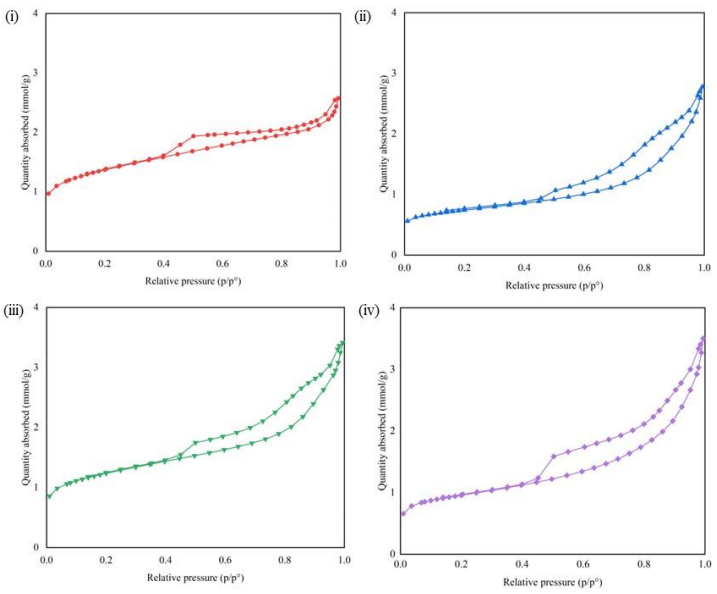

b) CA-0.002 (i), CA-0.004 (ii), CA-0.006 (iii), and CA-0.008 (iv): H2 loop

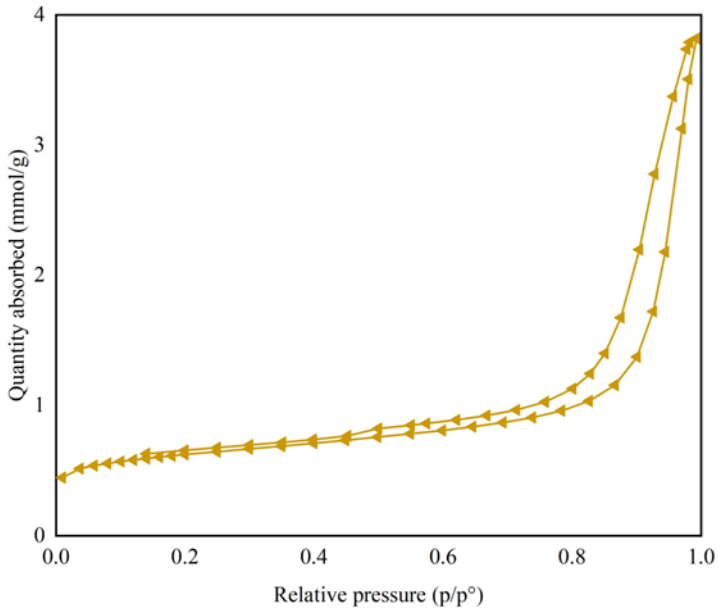

c) CA-0.01: H3 loop

Figure 4.8: Classification of N_2 Adsorption/Desorption Isotherm of Pure CA and CA-Mg Samples [a) Pure CA: H4 loop, b) CA-0.002 (i), CA-0.004 (ii), CA-0.006 (iii), and CA-0.008 (iv): H2 loop and c) CA-0.01: H3 loop]

Table 4.5: Summary of Glimpse of Pore Shape of Pure CA and CA-Mg Samples

Samples	Type of Hysteresis Loops	Pore Shape
CA	H4 loop	Narrow slit-shaped pores 
CA-0.002	H2 loop	Ink-bottled shape pores 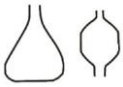
CA-0.004	H2 loop	Ink-bottled shape pores 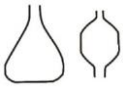
CA-0.006	H2 loop	Ink-bottled shape pores 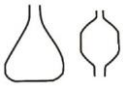
CA-0.008	H2 loop	Ink-bottled shape pores 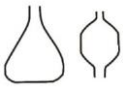
CA-0.01	H3 loop	Slit-like shape pores 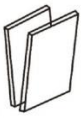

4.2.5 Morphology of Carbon Aerogel

The morphology of pure CA and CA-Mg samples was observed using FESEM images (Figure 4.9). Each sample with different concentrations showed different morphology in terms of porosity. For the pure CA sample, the structure was not well developed, and less pores were observed (Figure 4.9a). At 0.002 mol, the porosity increased with a well-structured structure, while at 0.004 and 0.006 mol, denser pores were observed. The structure drastically collapsed, and the porosity became more dense as the concentration increased to 0.008 mol and 0.01 mol (Figure 4.9 d,e,f). This is the major effect of the cross-linking reaction between Mg^{2+} and CMC molecules during aerogel synthesis. This reaction led to the formation of crosslinked network structures (Montes & Maleki, 2020).

During freeze-drying, the freezing method was applied to the samples. This may affect the structure of the ice formed, the water vapor during primary drying, and the quality of the final dried product. In Figure 4.9 (a,b,c), the samples might experience these effects, which caused them to have a network structure with large pores. It was recommended to work with high freezing rates to avoid internal diffusion of water vapor and form a more homogenous pore size distribution (Simón-Herrero et al., 2016). FESEM images (Figure 4.9) of the CA samples showed the differences in morphology of each sample in terms of porosity, where the density of porosity kept increasing as the concentration of Mg^{2+} increased. The differences can be observed in Table 4.4. The contribution of micropores was lessened as the concentration of Mg^{2+} increased. The increased contribution of mesopores helped in offering a good adsorption site for hydrogen.

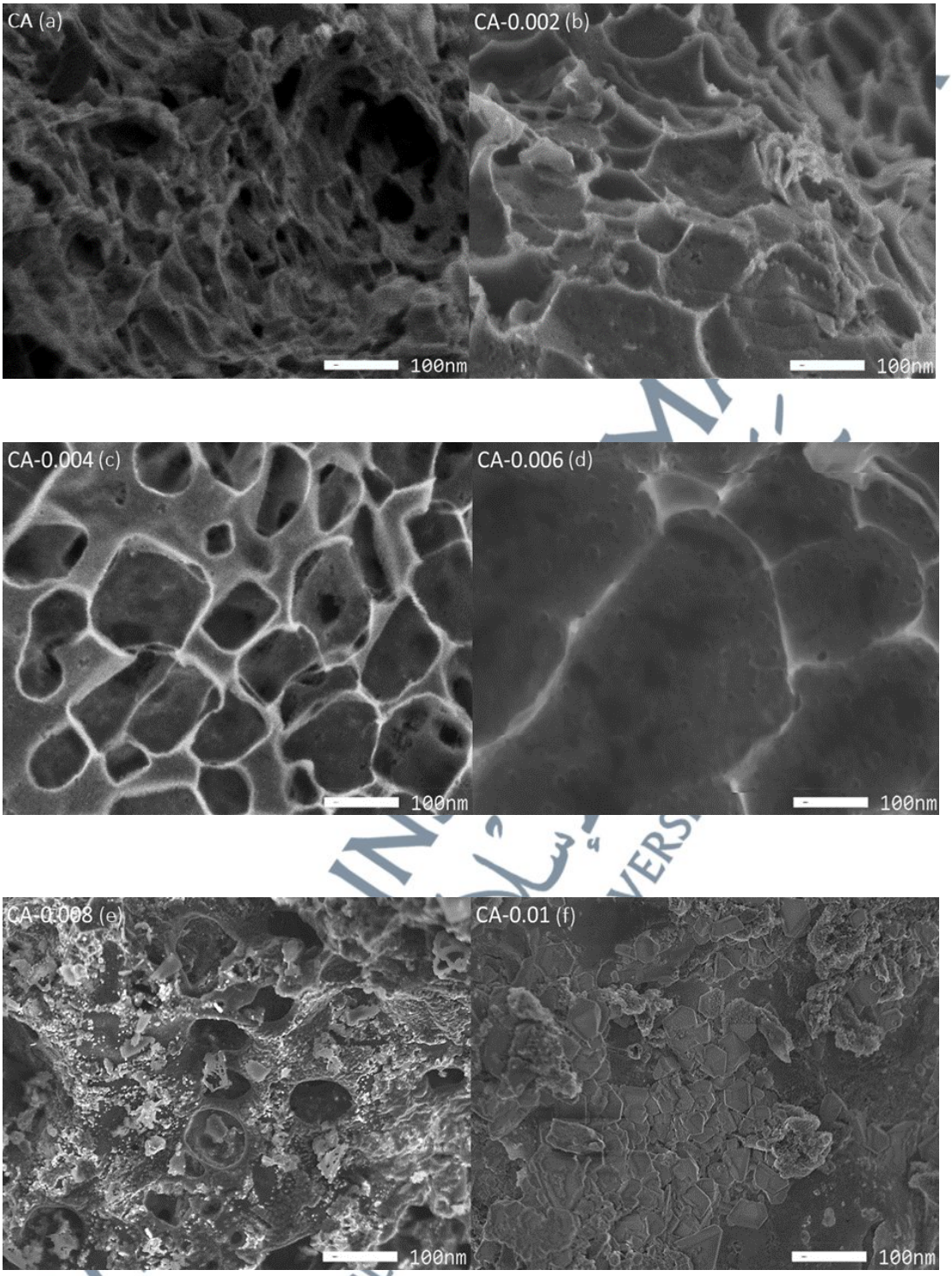

Figure 4.9: FESEM Images of a) CA, b) CA-0.002, c) CA-0.004 d) CA-0.006, e) CA-0.008 and f) CA-0.01

4.3 Conclusion

Commercial-grade CMC was used as the starting precursor in the synthesis of CA, and it was successfully crosslinked with all metal ions (Mg^{2+}, Mn^{2+}, Ni^{2+}, Zn^{2+}). Mg^{2+} was selected for further analysis as it fulfilled all the preliminary requirements to become a candidate for hydrogen storage material. With the addition of Mg^{2+}, the carbonisation of CA became more complete as the OH group disappeared from the FTIR spectra. This occurred due to the formation of MgO (periclase) during carbonisation as shown in the XRD pattern. The pore structure and size of pure CA and CA-Mg samples were further studied by using N_2 adsorption/desorption experiments and BET analysis, respectively. The sample of CA-0.01 possessed the highest value of pore volume, which is 0.1327 cm^3/g and the most probable pore size of 11.6339 nm. Besides, the presence of mesopores (pore sizes 2-50 nm) was determined based on the N_2 adsorption/desorption isotherm. The isotherm showed a clear hysteresis loop in the relative pressure region of $0.4 < P/P_o > 1.0$. The CA-0.01 sample exhibited the most likely feature of hydrogen storage material because it had the highest pore volume, and increased porosity, as shown in FESEM images where porosity increases as Mg^{2+} concentration increases with a slit-like shape pore. This feature might be a potential characteristic for CA as a hydrogen storage material.